JACS
JOURNAL OF THE AMERICAN CHEMICAL SOCIETY

Article

pubs.acs.org/JACS

Protein Biomineralized Nanoporous Inorganic Mesocrystals with Tunable Hierarchical Nanostructures

Xiang Fei,[†,‡,#] Wei Li,[§,#] Zhengzhong Shao,[†] Stefan Seeger,[‡] Dongyuan Zhao,[§] and Xin Chen*[,†]

[†]State Key Laboratory of Molecular Engineering of Polymers, Department of Macromolecular Science and Laboratory of Advanced Materials and [§]Department of Chemistry and Laboratory of Advanced Materials, Fudan University, Shanghai, 200433, P. R. China

[‡]Department of Chemistry, University of Zurich, Zurich, 8057, Switzerland

Supporting Information

ABSTRACT: Mesocrystals with the symmetry defying morphologies and highly ordered superstructures composed of primary units are of particular interest, but the fabrication has proved extremely challenging. A novel strategy based on biomineralization approach for the synthesis of hematite mesocrystals is developed by using silk fibroin as a biotemplate. The resultant hematite mesocrystals are uniform, highly crystalline, and porous nanostructures with tunable size and morphologies by simply varying the concentration of the silk fibroin and iron(III) chloride in this biomineralization system. In particular, we demonstrate a complex mesoscale biomineralization process induced by the silk fibroin for the formation of hematite mesocrystals. This biomimetic strategy features precisely tunable, high efficiency, and low-cost and opens up an avenue to access new novel functional mesocrystals with hierarchical structures in various practical applications.

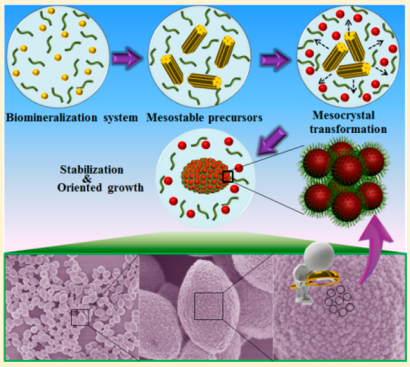

INTRODUCTION

Mesocrystals, a kind of assembled superstructure from nanocrystals in a crystallographically oriented way, have received rapidly increasing attention since they were first proposed by Cölfen and Antonietti in 2005.[1] Generally, the mesocrystals often have the symmetry defying morphology and exhibit highly ordered superstructure composed of several to hundreds of primary units formed by mesoscale transformation induced by template additives. It usually possesses new collective properties and advanced tunable functions arising from subunits ensembles.[2] In nature, biological systems provide an ideal mesoscale transformation when synthesizing mesocrystal biominerals, such as bone, teeth, shells, sea urchin spikes, and aragonite tablets in nacre. This is a well-known biomineralization process, which is highly sophisticated in terms of its adaptation to function.[3] Inspired by nature, biological synthesis of mesocrystals with a precise control ability has attracted extensive attention both in academia and industry in recent years.[4]

As a special case of functional metal oxides, iron oxide is of great interest because of its multiple applications in diverse areas. Among iron oxides, hematite (α-Fe_2O_3) is the most thermodynamically stable semiconductor (E_g = 2.1−2.2 eV), and the corresponding hematite nanomaterials have been extensively studied due to their wide range of applications, including light-induced water splitting,[5] solar cells,[6] lithium-ion batteries,[7] catalysts,[8] and biotechnology.[9] In general, the properties and practical performance of hematite nanomaterials are highly dependent on their crystal phase, crystallinity, surface area, porosity, morphology, and nanostructure. In this regard, hematite mesocrystals with tunable architecture would provide many new opportunities to design functional materials. However, the synthesis of mesocrystals with highly sophisticate superstructure arising from precise assembly of the subunits by conventional methods is still challenging. For example, it requires matching the precise reaction between the additives and the iron oxide precursors when preparing hematite mesocrystals, which is somewhat beyond the typical crystal growth mechanism. Therefore, it is highly desired to develop a simple and versatile strategy for the synthesis of hematite mesocrystals with tunable nanostructures.[10]

Silkworm silk, produced by *Bombyx mori* silkworm, has been used in the textile industry for 5000 years.[11] In the last few decades, *B. mori* silk fibroin has attracted increasing attention from scientists and engineers owing to its diverse applications in functional materials and biomedical fields.[12] As an appealing biopolymer, silk fibroin possesses unique sequence-specific self-assembly behavior and substrate recognition property,[13] acting as a diverse biotemplate for the synthesis of inorganic nanomaterials with controllable morphology and polymorphs. We have already prepared several kinds of inorganic nanomaterials, such as calcium carbonate, noble metal, and metal oxide nanomaterials in the past few years.[14]

In this article, we report a biological strategy to synthesize the hematite mesocrystals by using silk fibroin as a biomineralization template via a facile hydrothermal method. Briefly, silk fibroin was first incubated with ferric chloride as a biotemplate. Afterward, the whole system was heated 160 °C, triggering the crystal transformation and oriented assembly of

Received: September 10, 2014
Published: October 17, 2014

   dx.doi.org/10.1021/ja509334x | J. Am. Chem. Soc. 2014, 136, 15781−15786

primary hematite nanocrystals. The obtained hematite mesocrystals have a uniform, highly crystalline, and porous nanostructure. The size and morphology of these hematite mesocrystals can be tunable by simply varying the concentration of silk fibroin and $FeCl_3$ in such a biomineralization system. We also revealed a complex mesoscale biomineralization process including the controllable nucleation and growth of hematite nanocrystals from the dissolution of metastable solid goethite precursors as well as the stabilization and oriented-assembly of the primary hematite nanoparticles with silk fibroin to a biomineralized hematite mesocrystal. Finally we showed a practical application of such a hematite mesocrystal, an oxygen evolution photocatalyst in water splitting system. The performance of the hematite mesocrystals was much better than its single-crystal counterparts in the visible-light-driven $[Ru(bpy)_3]^{2+}$-persulfate system.

RESULTS AND DISCUSSION

Characterization and Morphology of the Hematite Mesocrystal. The X-ray diffraction (XRD) pattern and X-ray photoelectron spectroscopy (XPS) analyses (Figures S1 and S2) show that the samples prepared by silk fibroin-biomineralization method are pure hematite (α-Fe_2O_3) without any other phase such as Fe_3O_4 and γ-Fe_2O_3. Field-emission scanning electron microscopy (FESEM) and transmission electron microscopy (TEM) provide insights into the morphology and detailed structure of the samples. The typical olive-like particles with predominantly about 620 × 940 nm in short and long axis length can be found in low-magnified SEM images (Figure 1a). A closer observation, as shown in Figure 1b,c, displays that each particle is relatively rough and apparently builds from primary nanoparticles (mesocrystal subunits) with the diameter of 5−10 nm. TEM images further confirm the morphologies of the hematite nanomaterials are through an oriented growth with primary nanoparticles (Figure 1d,e). As seen from Figure 1e, clear gaps between primary nanoparticles can be observed. Due to the dense aggregation of the primary nanoparticles, the stacked interiors are not distinct. The related selected area electron diffraction (SAED) pattern obtained from the edge (circle area) of the particle exhibits a typical single-crystal spot pattern (inset in Figure 1e), suggesting that the whole assembly of the primary hematite nanoparticles is highly oriented. The diffraction spots are slightly elongated, indicating a small lattice mismatch between the boundaries of the nanoparticles when they are assembled in the same orientation, typical for mesocrystals.[1,10]

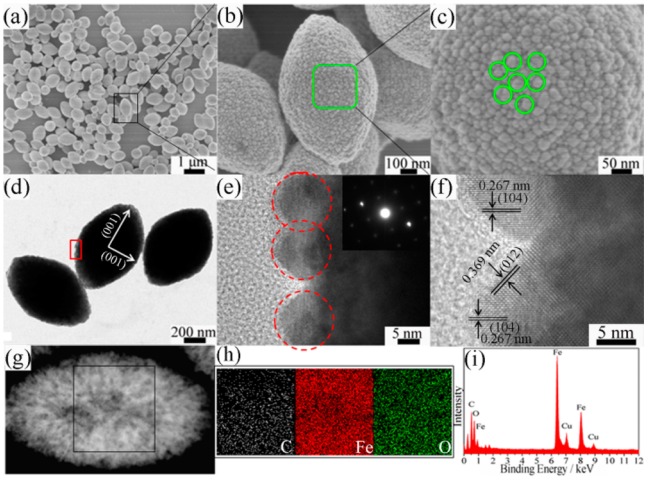

Figure 1. (a−c) FESEM images of the olive-like hematite mesocrystal obtained after 10 h in the silk fibroin biomineralization system ([RSF] = 0.1 wt %, [Fe(III)] = 0.06 mol/L). (d, e) TEM image of the same hematite mesocrystal, and the inset in (e) shows the SAED pattern. (f) HRTEM image of the primary hematite nanoparticles. (g) HAADF-STEM image of a single olive-like hematite particle. (h) EDS mapping images of C, Fe, and O for the square region of the single hematite particle in (g). (i) EDX spectrum of the olive-like hematite mesocrystal, where the signals of C and Cu are generated from the Cu grids and carbon support film, respectively.

A representative high-resolution TEM (HRTEM) image is presented in Figure 1f, from which the (104) lattice spacing (0.267 nm) and the (012) lattice spacing (0.369 nm) of rhombohedral hematite can be clearly observed. In addition, the high-angle annular dark-field scanning TEM (HAADF-STEM) image (Figure 1g) confirms the porous nature of the hematite nanomaterials. Elemental mapping by energy-dispersive X-ray spectroscopy (EDS) shows that the elements C, Fe, and O are homogeneously distributed throughout the whole hematite particle (Figure 1h), which illustrates the existence of silk fibroin (the source of element C) in the hematite mesocrystals. Furthermore, thermogravimetric analysis (TGA) was carried out in air to reveal the content of silk fibroin biotemplate (Figure S3). Two dominant weight losses of about 2.4 wt % in total due to the thermal decomposition of the silk fibroin are observed in the range of 200−800 °C. The first slight weight loss of about 0.25 wt % below 150 °C was assigned to the elimination of water in the material. These results suggest, as expected, that the silk fibroin biotemplate is involved in the biomineralization process and homogeneously distributed throughout the whole hematite mesocrystal. In addition, the porous nature of the hematite mesocrystals was also confirmed by nitrogen sorption measurements (Figure S4). These olive-like hematite mesocrystals give rise to Brunauer−Emmett−Teller (BET) surface area of 11.4 m^2/g (Figure S4a) with an average pore size of about 5 nm, calculating by the Barrett−Joyner−Halenda (BJH) method (Figure S4b). The uniform nanopore is mainly contributed to the aggregation voids of the nanometer-sized hematite primary nanoparticle subunits.

Mesoscale Transformation of the Hematite Mesocrystal. To shed light on the formation mechanism of the silk fibroin biomineralized hematite mesocrystals, SEM and XRD technologies were used to monitor the time-dependent evolution process, and the results are shown in Figures 2, S5, and S6. Nanoneedles were the dominant products within 1.5 h of reaction, and their size increased with the time (Figure 2a,b). Few nanobundles can be found in the high-magnification SEM image at this stage (inset in Figure 2b). The corresponding XRD patterns (Figure S5) indicate that these nanoneedles are assigned to the pure orthorhombic goethite (α-FeOOH, JCPDS no. 29-0713, space group *Pnma*, a = 9.95 Å, b = 3.01 Å, c = 4.62 Å).[15] Along with the reaction proceeding to 1.5 h (Figure 2c), the hierarchical nanobundles composed of abundant nanoneedles were formed (Figure 2c) and simultaneously tend to transform to olive-like particles with a size of about 350 × 600 nm (a new formed olive-like particle can be found in the inset of Figure 2c). The corresponding XRD pattern indicates that the goethite is still the main product in this stage (Figure S5).

In order to capture the change of nanoneedles to olive-like particles, we shortened the reaction time interval for 10 min

dx.doi.org/10.1021/ja509334x | J. Am. Chem. Soc. 2014, 136, 15781−15786

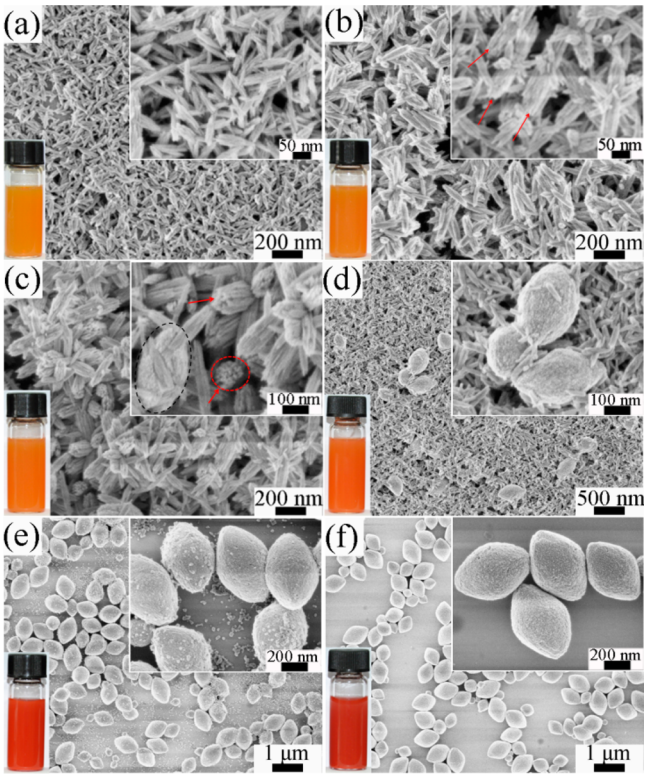

Figure 2. FESEM images of the time-dependent evolution in the form of the olive-like hematite mesocrystal obtained after 10 h in the silk fibroin biomineralization system ([RSF] = 0.1 wt %, [Fe(III)] = 0.06 mol/L): (a) 0.5, (b) 1, and (c) 1.5 h; (d) 1 h 40 min; (e) 1 h 50 min; and (f) 2 h. The insets show larger scale panoramic views of the structures.

after 1.5 h of reaction. Figure 2d,e demonstrates that more olive-like particles are formed with the increase of time. In addition, we did find the intermediate stage of the transformation from goethite to hematite at 1 h 40 min as both the SEM image and XRD pattern clearly indicate the coexistence of α-FeOOH and α-Fe_2O_3 crystalline phase (Figures 2d and S5). The olive-like particles were formed and α-Fe_2O_3 crystalline phase became dominated when the reaction reached 1 h 50 min (Figures 2e and S5). The phase transformation during the reaction process is attributed to the dehydration of metastable α-FeOOH under the hydrothermal condition that has been proved in the previous studies.[15] When the reaction time was prolonged to 2 h, the transformation of α-FeOOH nanobundles to α-Fe_2O_3 olive-like particles was complete (Figure 2f). Further extending the reaction time (4 h or even longer) barely changed the shape and size of the α-Fe_2O_3 mesocrystals (Figures S5 and S6).

It is noteworthy that the intermediate stage of transformation is very short, and the olive-like hematite particles are formed within 20 min in such a silk fibroin biomineralization system. The crystalline transformation and oriented growth of nanoparticles occur simultaneously during the formation of the unique hematite mesocrystals in this biomineralization system. That is, the metastable α-FeOOH nanobundles act as the precursors for the subsequent nucleation and growth of hematite nanocrystals, and then the primary hematite nanoparticles are stabilized and oriented for the aggregation along the [001] direction to form the olive-like hematite mesocrystals induced by the silk fibroin.

In our previous research, we also found the same phenomenon when we used silk fibroin to direct the growth of aragonite crystals.[14b] We assumed the reason is the relatively poor interactions between the silk fibroin template and the (001) faces of the crystal. Actually, the similar crystal growth pattern is also found in other mesocrystals, for example, anatase TiO_2 mesocrystals,[16] but the exact mechanism is still unsolved.

We find the Fe(III) concentration is a critical role for the formation of hematite mesocrystals. Only when Fe(III) concentration reaches a certain value (0.06 mol/L), hematite mesocrystals can be readily formed (Figure S7). Low Fe(III)concentration ([Fe(III)] = 0.01 or 0.02 mol/L) produces hematite nanospheres with a uniform size of about 50 or 100 nm (Figure S7a,b). Such nanospheres, as reported in our previous work,[14e] follow different evolution process. When Fe(III) concentration increased to 0.04 mol/L, the olive-like hematite particles (about 200 × 400 nm) emerged (Figure S7c), which maybe the startup for the formation of mesocrystals but is still not the mature one. Further increase in Fe(III) concentration produced hematite mesocrystals with larger size (Figure S7e). Therefore, to increase the Fe(III) concentration in such a silk fibroin biomineralization system, we can obtain hematite particles from nanospheres to mesocrystals (Figure S7f).

The Effect of the Silk Fibroin Concentration on Biomineralized Hematite. According to the principle of biomineralization, biotemplates (such as special proteins and peptides) play multiple roles in directing the formation of the complex inorganic nanomaterials, including composition, morphology, and structure.[4c] To investigate the crucial role of the silk fibroin in this biomieralization system, a series of experiments were designed by varying the silk fibroin concentration from 0 to 0.5 wt % with a constant Fe(III) concentration of 0.06 mol/L. A remarkable dependence of the crystal morphology on the concentration of the silk fibroin was observed, and representative SEM images of the biomineralized hematite nanomaterials are shown in Figure 3. As a control, hematite monocrystal cubes (about 900 nm in size) with comparatively smooth surface feature were obtained without the addition of silk fibroin (Figure S8). At a very low silk fibroin concentration ([RSF] = 0.01 wt %), uniform spindle-like hematite particles were formed (Figure 3a) with roughly middle part and smooth ends, which is clearly shown in the inset of Figure 3a. It is very interesting that both monocrystal and mesocrystal regions exist in one single hematite particle. When the silk fibroin concentration increased to 0.02 wt %, the spindle-like hematite particles exhibited a larger rough mesocrystal region in the middle part (Figure 3b). Such an evolution continued as the silk fibroin concentration increased to 0.05 wt % (Figure 3c). The whole particle almost shows the mesocrystal architecture and only a very little monocrystal architecture could be found in the ends (Figure 3c). In addition, the shape of the hematite particles began to change to olive-like as the typical concentration ([RSF] = 0.1 wt %) as discussed above. The shape and architecture of the hematite particles obtained from [RSF] = 0.1 and 0.2 wt % were similar (Figure 3d,e) but changed to a larger ellipsoidal one if the silk fibroin concentration increased to 0.5 wt % (Figure 3f).

As a summary, the structure of the final hematite products evolves as the following sequence when we performed a typical synthesis with a constant Fe(III) concentration of 0.06 mol/L: from a spindle-like particle with both monocrystal and mesocrystal architecture to an olive-like mesocrystal and finally

dx.doi.org/10.1021/ja509334x | J. Am. Chem. Soc. 2014, 136, 15781−15786

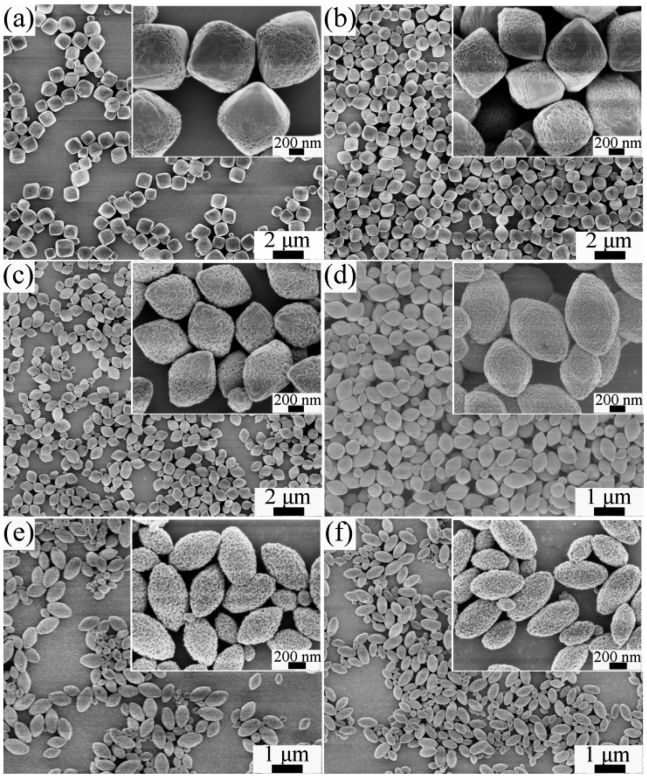

Figure 3. FESEM images of the biomineralized hematite nanomaterials obtained after 10 h with a constant Fe(III) concentration (0.06 mol/L) by varying silk fibroin concentration: (a) 0.01, (b) 0.02, (c) 0.05, (d) 0.1, (e) 0.2, and (f) 0.5 wt %. The insets show larger scale panoramic views of the structures.

to an ellipsoidal mesocrystal by gradually increasing the initial silk fibroin amount (Figure 3). In order to characterize the morphological change of these hematite particles semi-quantitatively, we defined the length of the long and short axes of the particles to l and d and the height of the rough middle part (mesocrytal) to h (Figure S9a). Generally, it can be separated to two structure regions (Figure S9b), one is the coexistence of monocrystal and mesocrystal architecture in one single hematite particle, another is the completely hematite mesocrystal structure. To be specify, in the first region with low silk fibroin concentration ($0 < [RSF] < 0.1$ wt %), the h value increased from about 430 to 750 nm and l/h decreased from 1.83 to 1.25 with the increase in silk fibroin concentration. In second region ($[RSF] \geq 0.1$ wt %), the h value was equal to l (i.e., the value of l/h decreased to a constant of 1). All these data imply that silk fibroin plays an important role during the formation of hematite particles, which makes it possible to precisely regulate the hierarchical nanostructures and then tune the architectures.

Formation Mechanism of Silk Fibroin-Biomineralized Hematite Mesorystals. The mesoscale formation process of hematite mesocystals in the silk fibroin biomineralization system is assumed in Scheme 1. First, Fe(III) ions can form a complex with silk fibroin by interaction with tyrosine and other polar amino acid residues, which is well-known. Because silk fibroin is a fibrous protein, it can be imagined that the Fe(III) ions attach on the long and relatively extended protein chain. Then, the Fe(III)-silk fibroin complexes are hydrolyzed into metastable goethite nanoneedles during the initial hydrothermal process and concurrently assemble into goethite

Scheme 1. Schematic Illustration on the Biomineralization Process of the Hematite Mesocrystals

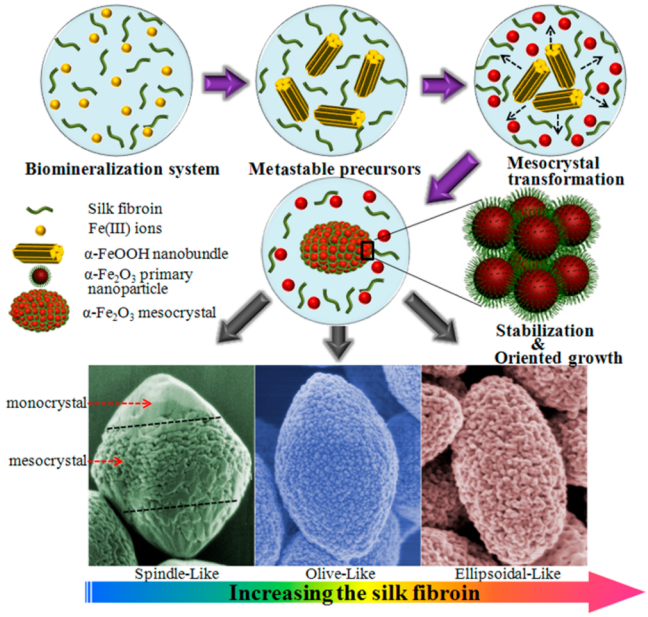

nanobundles as a result of the strong interaction between amino acid residues and Fe(III) ions.[17] Subsequently, goethite nanobundle precursors undergo dehydration transformation into primary hematite nanoparticles due to their instability under high temperature. They act as a reservoir to gradually release soluble iron-containing species for the growth of hematite nanoparticles via the Ostwald ripening. Due to the amphiphilic nature of silk fibroin and the strong interaction between its polypeptide chains and Fe(III) ions, silk fibroin would cover the surface of the primary hematite nanoparticles to decrease their surface energy, making them stable in the aqueous solution with a small particle size. Afterward, these primary nanoparticles assemble into larger nanoparticles and then form mesocrystals to further reduce the system energy mainly due to the self-assmbly of GAGAGS motifs in silk fibroin polypeptide chains. During the hydrothermal process, the whole silk fibroin macromolecular chain may degrade into several polypeptide segments at 160 °C, but it would not degrade into individual amino acids because the decomposition temperature should be higher than 200 °C (Figure S3). In the meantime, the most important GAGAGS motifs should remain in those segments as the previous thermal and enzyme degradation results already prove that the degradation starts at the amorphous region of silk protein. Therefore, if there is a certain degradation of silk fibroin during the synthesis process, the most important self-assembling ability of the silk protein would not be changed.

In this case, the interesting oriented assembly along the [001] direction maybe due to the relatively weak interaction between the silk fibroin and the (001) facets of hematite. However, at the low protein concentration, the silk fibroin is not enough to attach on all of the primary hematite nanoparticles. These protein-attached primary nanoparticles can still oriented assemble to form the mesocrystal architecture at the beginning, but after consuming all these nanoparticles, the continuous intrinsic crystal growth of hematite promotes the fusion of high-energy facets into a single crystal part in two ends of the final product, showing spindle-like shape. Although

dx.doi.org/10.1021/ja509334x | J. Am. Chem. Soc. 2014, 136, 15781−15786

the exact reason why the monocrystal formed in the two ends of the spindle-like particle is still not clear, we assume it should be the thermodynamically stable state for the combination of monocrystal and mesocrystal part in a single particle.

According to this assumption, it is easy to understand that if the silk fibroin concentration is high, more primary hematite nanoparticles are covered by silk fibroin, and the complete olive-like or ellipsoidal-like hematite mesocrystals are formed. On the other hand, with the increase of the concentration, more silk fibroin was covered on the primary hematite nanoparticles, which possibly speeds up the formation process of the hematite mesocrystals. That is because more initial mesocrystal "sites" can be created by the enhanced assembly ability from the increased number of protein chains. We did find that it took less time to form the stable hematite mesocrystals with more silk fibroin addition in the system, and as a result, the size of the final mesocrystals decreased accordingly (Figure 3).

Preliminary Study on Photocatalytic Performance of Hematite Mesocrystal. The performance of such hematite mesocrystals is demonstrated as a photocatalyst for water oxidation, which has been a demanding challenge in realizing a water splitting system. The initial photocatalytic water oxidation reaction was carried out in a Clark electrode system in the neutral pH buffer solution (potassium phosphate buffer system) with $[Ru(bpy)_3]^{2+}$ as sensitizer and sodium persulfate as a sacrificial electron acceptor.[18] As the Clark electrode only measures the oxygen concentration in the liquid phase, the total reaction time was set to 120 s, where the oxygen evolution does not go past its saturation point.

It is clearly shown in Figure 4 that the hematite mesocrystals exhibit enhanced oxygen evolution activity compared with the single-crystal hematite mirocubes with no silk fibroin addition.

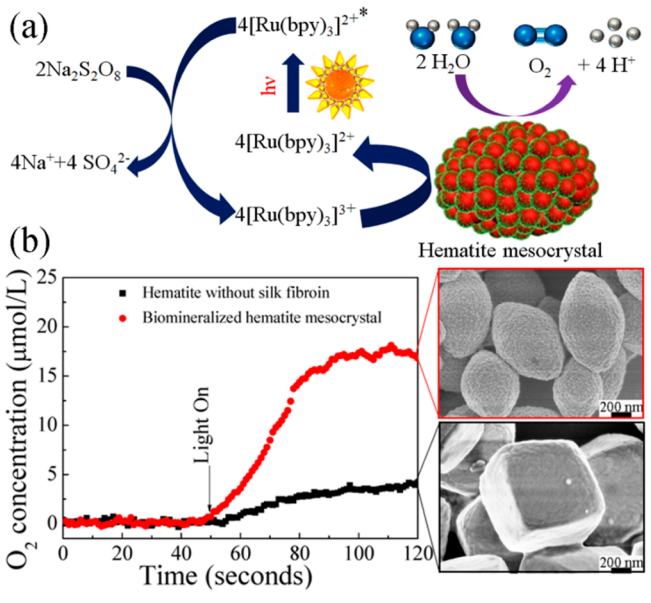

Figure 4. (a) Schematic of the photocatalytic water oxidation cycle with $Na_2S_2O_8$ as sacrificial electron acceptor, $[Ru(bpy)_3]^{2+}$ as photosensitizer, and the biomineralized hematite mesocrystal as catalyst. (b) Time courses of O_2 evolution under photo irradiation (LED lamp with 5500 Lux intensity, λ = 470 nm) in a phosphate buffer solution (pH 7.0, 8 mL) containing $Na_2S_2O_8$ (50 mg), $[Ru(bpy)_3]Cl_2$ (8 mg), and hematite nanomaterials (8 mg) at room temperature.

The specific catalytic activity of the olive-like hematite mesocrystals is 0.46 μmol O_2 L^{-1} s^{-1}, determined from the initial slope of the dissolved O_2 concentration, which is more than 5 times larger than that of the hematite microcubes (0.08 μmol O_2 L^{-1} s^{-1}). As the silk fibroin has no contribution to the water oxidation, we attribute the substantial enhancement of oxygen evolution activity to the high porosity of the hematite mesocrystals, which may improve the capability of the hexagonal hematite for holding four electrons to produce one oxygen molecule. The O_2 evolution activity of hematite mesocrystal can be calculated as 4.27 μmol/h here, though it is not very high compared with some other photocatalysts published, we use this as an example to demonstrate the relationship between the structure and the property of hematite particles.

CONCLUSIONS

We show that the nanoporous hematite mesocrystals with tunable size and morphology can be synthesized through a green, facile, and versatile route using silk fibroin as a biotemplate. This simple strategy, where all the constituents (Fe(III) source and silk fibroin) are incorporated in the initial solution and subsequently assemble in one step under 160 °C hydrothermal conditions, allows tailoring the final hematite mesocrystal matierials. A complex mesoscale biomineralization process involving the controllable nucleation and growth of the hematite nanocrystals from the dissolution of metastable solid goethite precursors, the stabilization and oriented assembly of primary hematite nanoparticles with silk fibroin is demonstrated for the formation of hematite mesocrystals. As an application example, we show the final hematite material exhibits good performance as a photocatalyst for water oxidation, which is attributed to the high porosity from its mesocrystal nature. As well as being interesting in itself, the biomass biomineralization methodology described here also provides a promising way for large-scale synthesis of functional mesocrystals, which is believed to be greatly desired in the energetic and environmental research fields.

EXPERIMENTAL SECTION

Preparation of Silk Fibroin Solution. Raw *B. mori* cocoon silk consists of fibroin fibers that are bound together by sericin, hydrophilic gum-like coat proteins. The degumming (removing the sericin) and dissolving process of *B. mori* silk followed previous procedures.[19] Then the silk fibroin solution was dialyzed against deionized water for 72 h at room emperature with a semipermeable membrane (MEMBRACEL, 12 000−14 000 MWCO) to remove LiBr. The dialyzed silk fibroin solution was centrifuged at 6000 r/min for 5 min, and the supernatant was collected at room temperature and stored at 4 °C. The concentration of the final silk fibroin solution was about 4 wt %.

Synthesis of Biomineralized Hematite Nanostructures. In a typical procedure, 3 mmol anhydrous $FeCl_3$ was added into 50 mL of 0.1 wt % silk fibroin solution ([RSF] = 0.1 wt %), in which the final Fe(III) concentration is 0.06 mol/L ([Fe(III)] = 0.06 mol/L), under continuous stirring for 0.5 h to form a transparent yellow aqueous solution. Then, the solution was transferred into a 100 mL Teflon-lined stainless-steel autoclave. The autoclave was heated to 160 °C and maintained for 10 h and then cooled to the room temperature. The final red precipitate was separated by centrifugation and then washed with distilled water three times and dried at 80 °C in air. The time-dependent experiment was carried out with the same recipe, i.e., [RSF] = 0.1 wt % and [Fe(III)] = 0.06 mol/L. To study the effect of Fe(III) concentration on the size and morphology, [RSF] was set to 0.1 wt %, and [Fe(III)] was varied from 0 to 0.08 mol/L. While investigating the

dx.doi.org/10.1021/ja509334x | J. Am. Chem. Soc. 2014, 136, 15781−15786

critical effect of silk fibroin, [Fe(III)] was set to 0.06 mol/L, and [RSF] was changed from 0 to 0.5 wt %.

Characterization. Powder XRD patterns were recorded on a Bruker D8 X-ray diffractometer (Germany) with Ni-filtered CuKα radiation (40 kV, 40 mA), employing a scanning rate of 0.02°/s in the 2θ range from 20 to 80°. FESEM images were obtained with a Hitachi S-4800 field emission scanning microscope (Japan) at 20 kV. TEM images were obtained with a Hitachi H-600 transmission electron microscope (Japan) at 75 kV. HRTEM, SAED, and electron diffraction (EDX) were performed on a JEM-2010F transmission electron microscope (JEOL, Japan) at an accelerating voltage of 200 kV. The XPS spectra were recorded in a vacuum ($<10^{-6}$ Pa) at a pass energy of 93.90 eV on a PerkinElmer PHI 5000C ESCA system (USA) equipped with a dual X-ray source using an MgKα (1253.6 eV) anode and a hemispherical energy analyzer. The binding energies obtained from XPS measurements were corrected by referencing the C 1s line to 284.5 eV. TGA was performed at 10 K/min on a Pyris 1 TGA instrument (Shimadzu DTG-60H) under an air atmosphere. Nitrogen adsorption−desorption isotherms were tested at 77 K with a Micromeritics Tristar 3020 analyzer. The samples were degassed under vacuum at 180 °C for at least 6 h before measurements. The specific surface areas were calculated using the BET method. The pore volumes and pore size distributions were obtained by using the BJH model from the adsorption branches of isotherms.

Water Oxidation Experiments. Photochemical water oxidation experiments were conducted in a 10 mL flask containing potassium phosphate buffer (8 mL, pH = 7), $[Ru(bpy)_3]Cl_2$ (8 mg) as photosensitizer, $Na_2S_2O_8$ (50 mg) as sacrificial electron acceptor, and the biomineralized hematite mesocrystals as catalyst (8 mg). The suspension was transferred to a 10 mL gastight vial and degassed with He to remove the dissolved oxygen contents. A 470 nm LED with 5500 Lux intensity was used as light source, and oxygen evolution was monitored with a calibrated Clark electrode. To eliminate any oxygen growth due to a possible air leak, the reactor was maintained in the dark for 30 min prior to irradiation, and no oxygen was observed.

■ ASSOCIATED CONTENT

Supporting Information

Additional XRD, XPS, TGA, BET, SEM, TEM characterization of the hematite products obtained at different conditions, the hematite size dependence on the Fe(III) concentration, and evolution models of biotemplated hematite nanomaterials. This material is available free of charge via the Internet at http://pubs.acs.org.

■ AUTHOR INFORMATION

Corresponding Author

chenx@fudan.edu.cn

Author Contributions

[#]These authors contributed equally to this paper.

Notes

The authors declare no competing financial interest.

■ ACKNOWLEDGMENTS

This work is supported by the National Natural Science Foundation of China (nos. 21034003 and 21274028). We thank Dr. Hongfei Liu at University of Zurich for the water oxidation experiments and valuable discussion. We also thank Dr. Bin Li, Mr. Yong Liu, Dr. Jinrong Yao, and Dr. Yuhong Yang at Fudan University for their precious suggestions and discussions.

■ REFERENCES

(1) (a) Cölfen, H.; Antonietti, M. *Angew. Chem., Int. Ed.* **2005**, *44*, 5576. (b) H. Cöelfen, Antonietti, M. *Mesocrystals and nonclassical crystallization*; John Wiley & Sons: Hoboken, NJ, 2008.

(2) (a) Talapin, D. V.; Lee, J. S.; Kovalenko, M. V.; Shevchenko, E. V. *Chem. Rev.* **2009**, *110*, 389. (b) Yuwono, V. M.; Burrows, N. D.; Soltis, J. A.; Penn, R. L. *J. Am. Chem. Soc.* **2010**, *132*, 2163. (c) Goesmann, H.; Feldmann, C. *Angew. Chem., Int. Ed.* **2010**, *49*, 1362.

(3) (a) Mann, S. *Nature* **1993**, *365*, 499. (b) Belcher, A.; Wu, X.; Christensen, R.; Hansma, P.; Stucky, G.; Morse, D. *Nature* **1996**, *381*, 56. (c) Cha, J. N.; Stucky, G. D.; Morse, D. E.; Deming, T. J. *Nature* **2000**, *403*, 289. (d) Naik, R. R.; Stringer, S. J.; Agarwal, G.; Jones, S. E.; Stone, M. O. *Nat. Mater.* **2002**, *1*, 169.

(4) (a) Kato, T. *Adv. Mater.* **2000**, *12*, 1543. (b) Nuraje, N.; Su, K.; Haboosheh, A.; Samson, J.; Manning, E. P.; Yang, N. l.; Matsui, H. *Adv. Mater.* **2006**, *18*, 807. (c) Dickerson, M. B.; Sandhage, K. H.; Naik, R. R. *Chem. Rev.* **2008**, *108*, 4935.

(5) (a) Warren, S. C.; Voïtchovsky, K.; Dotan, H.; Leroy, C. M.; Cornuz, M.; Stellacci, F.; Hébert, C.; Rothschild, A.; Grätzel, M. *Nat. Mater.* **2013**, *12*, 842. (b) Sivula, K.; Zboril, R.; Le Formal, F.; Robert, R.; Weidenkaff, A.; Tucek, J.; Frydrych, J.; Gratzel, M. *J. Am. Chem. Soc.* **2010**, *132*, 7436.

(6) (a) Zhou, H.; Wong, S. S. *ACS Nano* **2008**, *2*, 944. (b) Lin, Y.; Xu, Y.; Mayer, M. T.; Simpson, Z. I.; McMahon, G.; Zhou, S.; Wang, D. *J. Am. Chem. Soc.* **2012**, *134*, 5508.

(7) (a) Wang, B.; Chen, J. S.; Wu, H. B.; Wang, Z.; Lou, X. W. *J. Am. Chem. Soc.* **2011**, *133*, 17146. (b) Zhang, L.; Wu, H. B.; Madhavi, S.; Hng, H. H.; Lou, X. W. *J. Am. Chem. Soc.* **2012**, *134*, 17388. (c) Zhu, J.; Yin, Z.; Yang, D.; Sun, T.; Yu, H.; Hoster, H. E.; Hng, H. H.; Zhang, H.; Yan, Q. *Energy Environ. Sci.* **2013**, *6*, 987.

(8) (a) Weiss, W.; Ranke, W. *Prog. Surf. Sci.* **2002**, *70*, 1. (b) Zhou, X.; Lan, J.; Liu, G.; Deng, K.; Yang, Y.; Nie, G.; Yu, J.; Zhi, L. *Angew. Chem., Int. Ed.* **2012**, *51*, 178.

(9) Park, J.; An, K.; Hwang, Y.; Park, J. G.; Noh, H. J.; Kim, J. Y.; Park, J. H.; Hwang, N. M.; Hyeon, T. *Nat. Mater.* **2004**, *3*, 891.

(10) Song, R. Q.; Cölfen, H. *Adv. Mater.* **2010**, *22*, 1301.

(11) Sukigara, S.; Gandhi, M.; Ayutsede, J.; Micklus, M.; Ko, F. *Polymer* **2003**, *44*, 5721.

(12) (a) Tamura, T.; Thibert, C.; Royer, C.; Kanda, T.; Eappen, A.; Kamba, M.; Kômoto, N.; Thomas, J. L.; Mauchamp, B.; Chavancy, G. *Nat. Biotechnol.* **2000**, *18*, 81. (b) Shao, Z.; Vollrath, F. *Nature* **2002**, *418*, 741. (c) Altman, G. H.; Diaz, F.; Jakuba, C.; Calabro, T.; Horan, R. L.; Chen, J.; Lu, H.; Richmond, J.; Kaplan, D. L. *Biomaterials* **2003**, *24*, 401. (d) Tien, L. W.; Gil, E. S.; Park, S. H.; Mandal, B. B.; Kaplan, D. L. *Macromol. Biosci.* **2012**, *12*, 1671−1679. (e) Tao, H.; Kaplan, D. L.; Omenetto, F. G. *Adv. Mater.* **2012**, *24*, 2824. (f) Yun, Y. S.; Cho, S. Y.; Shim, J.; Kim, B. H.; Chang, S. J.; Baek, S. J.; Huh, Y. S.; Tak, Y.; Park, Y. W.; Park, S. *Adv. Mater.* **2013**, *25*, 1993. (g) Li, W.; Zhang, Z. H.; Kong, B.; Feng, S. S.; Wang, J. X.; Wang, L. Z.; Yang, J. P.; Zhang, F.; Wu, P. Y.; Zhao, D. Y. *Angew. Chem., Int. Ed.* **2013**, *52*, 8151.

(13) (a) Marsh, R. E.; Corey, R. B.; Pauling, L. *Biochim. Biophys. Acta* **1955**, *16*, 1. (b) Shen, Y.; Johnson, M. A.; Martin, D. C. *Macromolecules* **1998**, *31*, 8857.

(14) (a) Cheng, C.; Shao, Z.; Vollrath, F. *Adv. Funct. Mater.* **2008**, *18*, 2172. (b) Wang, T.; Porter, D.; Shao, Z. *Adv. Funct. Mater.* **2012**, *22*, 435. (c) Fei, X.; Jia, M.; Du, X.; Yang, Y.; Zhang, R.; Shao, Z.; Zhao, X.; Chen, X. *Biomacromolecules* **2013**, *14*, 4483. (d) Fei, X.; Shao, Z.; Chen, X. *Nanoscale* **2013**, *5*, 7991. (e) Fei, X.; Shao, Z.; Chen, X. *J. Mater. Chem. B* **2013**, *1*, 213.

(15) (a) Meng, F.; Morin, S. A.; Jin, S. *J. Am. Chem. Soc.* **2011**, *133*, 8408. (b) Navrotsky, A.; Mazeina, L.; Majzlan, J. *Science* **2008**, *319*, 1635.

(16) Ye, J.; Liu, W.; Cai, J.; Chen, S.; Zhao, X.; Zhou, H.; Qi, L. *J. Am. Chem. Soc.* **2010**, *133*, 933.

(17) (a) Waldo, G. S.; Theil, E. C. *Biochemistry* **1993**, *32*, 13262. (b) Fetter, J.; Cohen, J.; Danger, D.; Sanders-Loehr, J.; Theil, E. C. *JBIC, J. Biol. Inorg. Chem.* **1997**, *2*, 652.

(18) (a) Jiao, F.; Frei, H. *Angew. Chem., Int. Ed.* **2009**, *48*, 1841. (b) Hong, D.; Yamada, Y.; Nagatomi, T.; Takai, Y.; Fukuzumi, S. *J. Am. Chem. Soc.* **2012**, *134*, 19572.

(19) Chen, X.; Shao, Z.; Knight, D. P.; Vollrath, F. *Proteins: Struct., Funct., Bioinf.* **2007**, *68*, 223.